Elastic precursor softening in proper ferroelastic materials: A molecular dynamics study

Guangming Lu,[1,*] Francesco Cordero,[2] Kimura Hideo,[1] Xiangdong Ding,[3] Zhijun Xu,[1] Ruiqing Chu,[1] Christopher J. Howard,[4] Michael A. Carpenter,[5] and Ekhard K. H. Salje[5,†]

[1]*School of Environmental and Materials Engineering, Yantai University, Yantai 264005, China*

[2]*Istituto di Struttura della Materia-CNR (ISM-CNR), Area della Ricerca di Roma—Tor Vergata, Via del Fosso del Cavaliere 100, I-00133 Roma, Italy*

[3]*State Key Laboratory for Mechanical Behavior of Materials, Xi'an Jiaotong University, Xi'an 710049, China*

[4]*School of Engineering, The University of Newcastle, University Drive, Callaghan, New South Wales 2308, Australia*

[5]*Department of Earth Sciences, University of Cambridge, Cambridge CB2 3EQ, United Kingdom*

(Received 14 October 2023; accepted 29 January 2024; published 4 March 2024)

Precursor elastic effects are investigated in a displacive anharmonic spring model and shown to extend greatly into the paraelastic phase. Weak precursor effects can be detected near $2T_{tr}$, where T_{tr} is the ferroelastic transition temperature. The precursor effects become strong at $T < 1.7T_{tr}$. Two effects were identified in our two-dimensional model: the symmetry-breaking strain e_3 (ε_{xy}) leads to softening of the elastic modulus C_{33}, while the nonsymmetry-breaking strain $e_1 + e_2$ ($\varepsilon_{xx} + \varepsilon_{yy}$) leads to hardening of C_{11}. The strain e_3 is proportional to the order parameter and scales as $|e_1 + e_2| \sim e_3^2$. The temperature evolutions of the elastic moduli are surprisingly well described by power laws and Vogel-Fulcher equations. The power-law exponents are ~ -0.5 for ΔC_{33} and ~ -1 for ΔC_{11}, $\Delta(C_{11} + C_{12})$ and $\Delta(C_{11} - C_{12})$. The Vogel-Fulcher temperatures are very similar, while the Vogel-Fulcher energies differ between the excess elastic moduli. The origin of the precursor effect is the evolution of short-range order in the paraelastic phase which gives rise to a characteristic local nanostructure. In the case of the symmetry-breaking strain, this microstructure resembles dynamical twinning patterns corresponding to the ferroelastic nanostructure, which weakens the material. In the case of the nonsymmetry-breaking strain, we find density fluctuations which make the material harder.

DOI: 10.1103/PhysRevResearch.6.013232

I. INTRODUCTION

Most structural phase transitions show coupling between the order parameter and strain. The strain is directly proportional to the order parameter in some cases; in others, the relationship is described by coupling of various degrees of complexity [1–6]. Ferroelastic materials play a special role because the strain leads to the movement of domain boundaries and, thus, to the change of domain patterns [4]. They commonly display particularly large elastic anomalies during structural phase transitions [1], although the structural anomalies are also widely observed in nonferroic materials [7–11] and coelastic quartz [12]. Typical examples for structural collapses, which lead to an almost total reduction of the effective elastic moduli, are proper ferroelastics such as in $LaNbO_4$ and LaP_5O_{14} [13–15]. In the case of improper ferroelastics, such as ferroelectric $BaTiO_3$ and antiferrodistortive $SrTiO_3$, a linear coupling between the acoustic soft mode and the elastic moduli is symmetry forbidden, while elastic softening still reduces the values by 20–50% [16]. In ferroelectrics, the intrinsic softening of the low-temperature phase with respect to the paraelectric phase is due to the combined direct and converse piezoelectric effects [17,18]. Additional softening in the low-temperature phases may be due to mobile twin boundaries near the transition point, which vanishes if the twin walls are strongly pinned [19–21]. Thick domain walls were shown to be less prone to such pinning effects [22–24], and many examples of highly mobile wall movements during the softening process have been reported [25–30]. In a seminal paper, Cordero *et al.* [31] emphasized that elastic softening is not restricted to ferroic phases but that precursor elastic softening at temperatures well above the transition point is an indication of unexpected symmetry breaking at $T \gg T_c$. This softening has nothing to do with order parameter fluctuations and occurs outside any conceivable Ginzburg interval [32,33]. A typical example of a large precursor softening effect is the archetypical ferroelastic material $Pb_3(PO_4)_2$ [28,34]. The transition temperature in this slightly first-order transition is 453.6 K, while specific heat and strain precursors extend to 550 K. This is well above the transition point at $1.22T_{tr}$ in this displacive transition. The interval increases greatly to $1.5T_{tr}$ when order-disorder components are added by doping. Here, we find even greater precursor intervals in a carefully controlled displacive system.

*luguangming1990@ytu.edu.cn

†ekhard@esc.cam.ac.uk

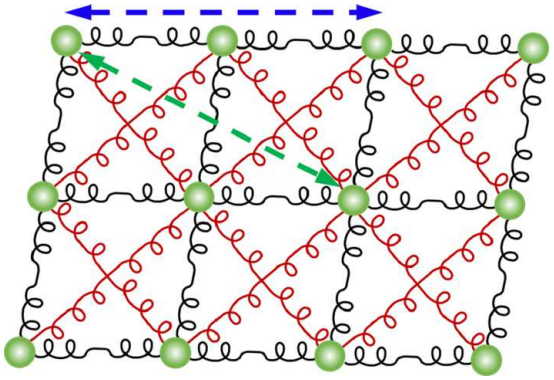

FIG. 1. Interatomic potential for a generic ferroelastic model. The model consists of nearest-neighbor (black springs), next-nearest-neighbor (red springs), third-nearest-neighbor (blue arrow), and fourth-nearest-neighbor (green arrow). The red springs are Landau springs with a double well potential so that the energy has a minimum value when the structure is sheared with respect to the cubic unit cell [52–58].

Similar precursor symmetry breaking was found by measuring the piezoelectric effect in nominally nonpiezoelectric phases [35] and by computer simulations of polymorphous local configurations in a broad range of materials [36–38]. It is the purpose of this paper to show by molecular dynamics (MD) calculations of a simple anharmonic spring model that elastic softening in addition to order parameter softening exists even in proper ferroelastic materials. Our model is purely displacive, while conceptually, this effect is best visualized when materials are disordered by extrinsic forces such as radioactive bombardment. Consider a single crystal without any domain boundaries which is disordered by the radioactive decay of radiogenic impurities. This situation is encountered in so-called metamict materials such as zircon [39] and titanite [40], where the reduction in bulk and shear modulus is >50%, while their crystallographic average structure is still unchanged. Structural disorder of the paraelastic phase and significant short-range order are thus expected to lead to elastic softening and piezoelectricity in nominally cubic materials [35,38,41–43], although the structural reason for the elastic softening is often subtle [38]. We show that precursor softening is not limited to order-disorder systems but also appears in displacive systems [44–51].

II. THE MODEL

Ferroelastic materials and related precursor elastic effects induced by the presence of local dynamic ferroelastic nanostructures above the Curie temperature are described by a Landau-type double-well potential on the interatomic interactions, as schematically shown in Fig. 1. The potential energy $U(r)$ contains four terms: the harmonic first-nearest atomic interactions:

$$U(r) = 0.1(r-1)^2 \quad \text{(black springs)}, \tag{1}$$

the anharmonic second-nearest Landau-type double-well interactions:

$$U(r) = -0.05(r-\sqrt{2})^2 + 40(r-\sqrt{2})^4 \quad \text{(red springs)}, \tag{2}$$

along diagonals in the lattice unit, the fourth-order third-nearest interactions:

$$U(r) = 0.04(r-2)^4 \quad \text{(blue arrow)}, \tag{3}$$

and another anharmonic fourth-nearest Landau-type double-well interaction:

$$U(r) = -0.05(r-\sqrt{5})^2 + 25.5(r-\sqrt{5})^4 \quad \text{(green arrow)}, \tag{4}$$

where r is the distance between atoms. The first- and third-nearest interactions are related to the elastic interactions and constitute the elastic background in ferroelastic materials. An equilibrium shear angle of 2° is maintained by the second-nearest interactions, while the additional fourth-nearest Landau-type interactions help to obtain a reasonable domain wall thickness and stability [27,59]. The model parameters were inspired by the well-known second-order phase transition of $SrTiO_3$ with a typical ferroelastic shear angle of 2° [60]. The simulated microstructures are fairly robust with respect to the parameters in Eqs. (1)–(4). The parameters were optimized to reproduce a weakly first-order transition where the temperature evolution of the order parameter is smooth in the ferroelastic phase and shows a step at the transition temperature. Similar potential forms have been developed to successfully investigate internal frictions accompanying the dynamic motions of ferroelastic domains [21,52], the interactions of fine microstructures inside the domain walls [53,54], piezoelectricity [55,56], ferroelectricity [57], and magnetism [58] emerging from the static and dynamic polar ferroelastic domain walls (often simple twin walls) [61,62]. Ferroelastic domain patterns and stress-field-induced strains were obtained by extracting structural snapshots every 10 MD steps (0.01 ps) in the last 1.5×10^6 MD steps. All simulations are performed using the LAMMPS code [63]. Visualizations are performed using the OVITO software [64].

A formal treatment of the symmetry properties of the model is presented in the Appendix. In its high-symmetry state, the spring model has symmetry which conforms to plane group $p4mm$. The distorted structure shown in Fig. 1 has the symmetry of one of the subgroups of this, namely, $c2mm$. The Appendix also identifies symmetry-adapted combinations of spontaneous strains and elastic moduli for the model, in Voigt notation.

To avoid surface effects in our two-dimensional (2D) model, periodic boundary conditions were adopted in both x and y directions. We set the equilibrium lattice parameters along the x and y directions before relaxation to $a = 1$ Å $=$ 1 lattice unit (l.u.) for the sample size of 500 × 500 l.u. The atomic mass is $M = 100$ amu. At each temperature step, the related structure was relaxed for 3×10^6 MD steps (3×10^3 ps) to allow enough time for the potential nucleation and relaxation of local precursor ferroelastic domains. The sample temperature and pressure were controlled by using the Nosé-Hoover thermostat method [65,66], known as the NPT

ensemble, which allows the sample shape and size to change freely under external stresses. Shear and tensile stresses (σ_3 and σ_1, σ_2) were then applied to the sample. The stress-field-induced strains e_3 and e_1, e_2 under each well-defined applied stress were calculated by averaging the box length and shear angle. Elastic moduli C_{ik} ($i, k = 1,2,3$) were then determined by linear fittings. We have simulated the elastic stiffness constant matrix of the paraelastic phase [Eq. (1)] at a temperature of $T = 2.625T_{tr}$, where T_{tr} is the phase transition temperature of the 2D model:

$$\begin{pmatrix} C_{11} & C_{12} & C_{13} \\ C_{21} & C_{22} & C_{23} \\ C_{31} & C_{32} & C_{33} \end{pmatrix} = \begin{pmatrix} 72.88 & 22.80 & 0.05 \\ 22.79 & 72.72 & 0.14 \\ 0.04 & 0.09 & 23.24 \end{pmatrix} \text{Gpa}. \tag{5}$$

The symmetry of this elastic constant matrix is, within computational uncertainty, that expected for a structure in *p4mm* (see Appendix). This confirms the square symmetry of the paraelastic phase described by the model.

III. RESULTS

The transition behavior of our 2D spring model was first characterized. The simulation started from an initial single ferroelastic domain state with a shear angle of 2°, i.e., with a spontaneous shear strain $e_3 = 0.035$. This was then followed by a continuous heating process from $0.027T_{tr}$ to $2.625T_{tr}$, where T_{tr} is ~0.362 K in the model. The transition temperature is very low because the displacive limit of the model is 0 K [67]. Renormalization of the phonon branches increases T_{tr} slightly. To use scale-independent temperatures, we measured all temperatures in this model in units of T_{tr}. To capture the elastic precursor softening, we cooled stepwise the high-temperature paraelastic phase from $2.625T_{tr}$ [A in Fig. 2(a)] into the low-temperature ferroelastic phase at $0.027T_{tr}$ [B in Fig. 2(a)]. Figure 2(a) shows the temperature evolution of the potential energy with a step at T_{tr}. The deviation from the displacive limits originates from the spontaneous formation of nanostructures which drive the system from harmonic soft modes to anharmonic excitations. The microstructures of high-symmetry paraelastic and low-symmetry ferroelastic phases are shown in Figs. 2(b) and 2(c). Uniform zero strain exist at A in Fig. 2(b) and typical ferroelastic stripe domains at B in Fig. 2(c).

The change of relevant strain parameters as a function of temperature is shown in Fig. 3(a) with the branch of the positive shear strain $+e_3$ and negative shear strain $-e_3$, the averaged shear strain $\langle e_3 \rangle$. The shear strain e_3 is the symmetry-breaking strain of the sample which would cancel in an infinite sample with an equal number of domains with positive and negative shear. However, since the symmetry of our simulation box is not perfect, there is a slight asymmetry between negative and positive shear strains and a small but finite averaged shear strain $\langle e_3 \rangle$. Figure 3(b) shows the evolution of the smaller, nonsymmetry-breaking area strain $e_1 + e_2$ as a function of temperature with a step at T_{tr}. Because the positive and negative shear strains are not symmetrical, a small area anomaly at T_{tr} has been obtained, as shown in Fig. 3(c). The

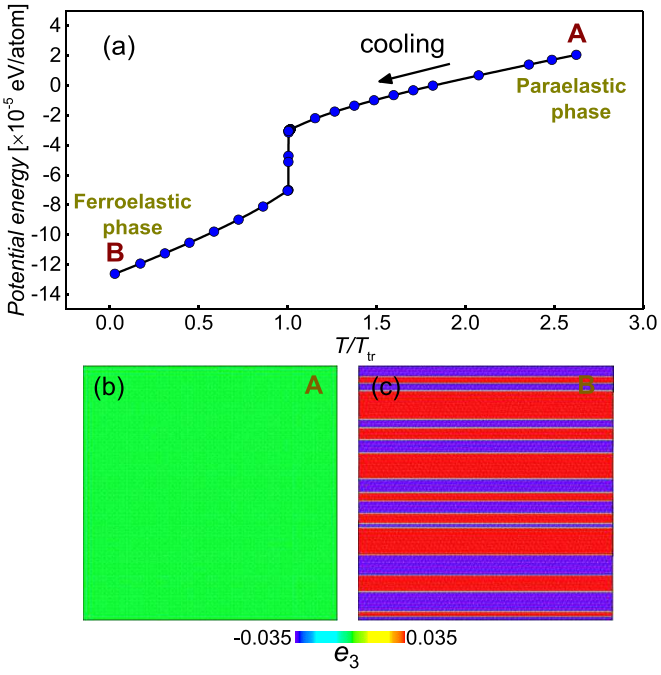

FIG. 2. Potential energy change upon decreasing the system temperature (a). The ferroelastic phase transition temperature is T_{tr}. (b) Microstructure of the paraelastic phase at A. (c) Microstructure of the ferroelastic phase at B. The colors are coded by the atomic-level shear strain (e_3).

correlation between e_3 and $e_1 + e_2$ is $e_3^2 \sim e_1 + e_2$ [Fig. 3(d)]. The log-log scale in Fig. 3(e) confirms the exponent of 2.

The evolution of the shear (C_{33}) and tensile (C_{11}) elastic moduli under decreasing temperature is shown in Fig. 4. Each data point was determined by calculating the slopes of the Hooke's law linear correlations of applied stresses and induced strains. Figures 4(a) and 4(c) show the dependences of C_{33} and C_{11} on temperature over the full temperature range, while Figs. 4(b) and 4(d) are magnifications of the elastic moduli between $1.0T_{tr}$ and $1.9T_{tr}$, as indicated by A and B in Fig. 4. The overall temperature dependence is that of a proper ferroelastic material [1] with the linear temperature dependence at $T \gg T_{tr}$ showing the softening of the acoustic phonon branch. This classic softening is superimposed by additional softening of C_{33} and hardening of C_{11} when approaching the transition temperature. The softening visibly extends in the graphs to $\sim 1.7T_{tr}$ and shows an asymptotic convergence toward the background linear temperature dependence at higher temperatures. We do not observe any singularity which could be understood as a typical Burns temperature [68], in agreement with several recent experimental observations [18].

Based on the data in Fig. 4, we calculated deviations of the elastic moduli from the linearly fitted values (represented by red lines in Fig. 4) [ΔC_{11}, ΔC_{33}, $\Delta(C_{11} + C_{12})$ and $\Delta(C_{11} - C_{12})$], which corresponds to the additional softening and hardening of related elastic moduli induced by the presence of precursor domains as approaching the transition temperature. The evolution of ΔC_{11}, ΔC_{33}, $\Delta(C_{11} + C_{12})$ and $\Delta(C_{11} - C_{12})$ as a function of temperature is shown in Fig. 5.

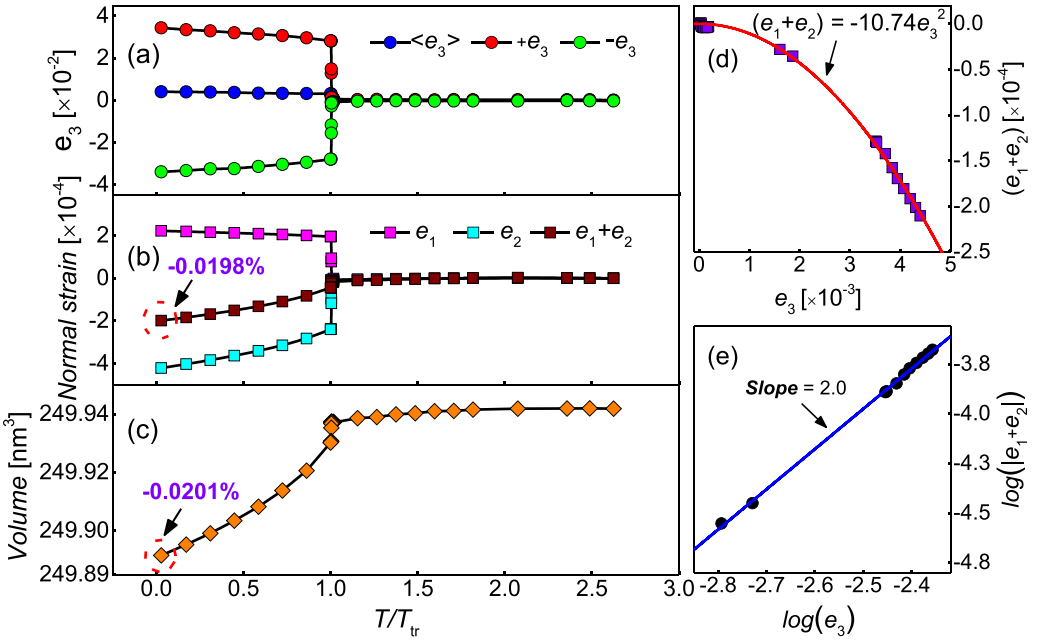

FIG. 3. Primary and secondary strain order parameter evolutions as function of temperature. (a) Positive ($+e_3$), negative ($-e_3$). and averaged ($\langle e_3 \rangle$) shear strain as a function of temperature. (b) e_1 and e_2 as a function of temperature. (c) System volume (500×500×1 unit cells with edge dimensions of ∼0.1 nm) as a function of temperature. (d) Parabolic scaling $e_1 + e_2 \sim e_3^2$. (e) Log-log plot for the normal strain and positive shear strains.

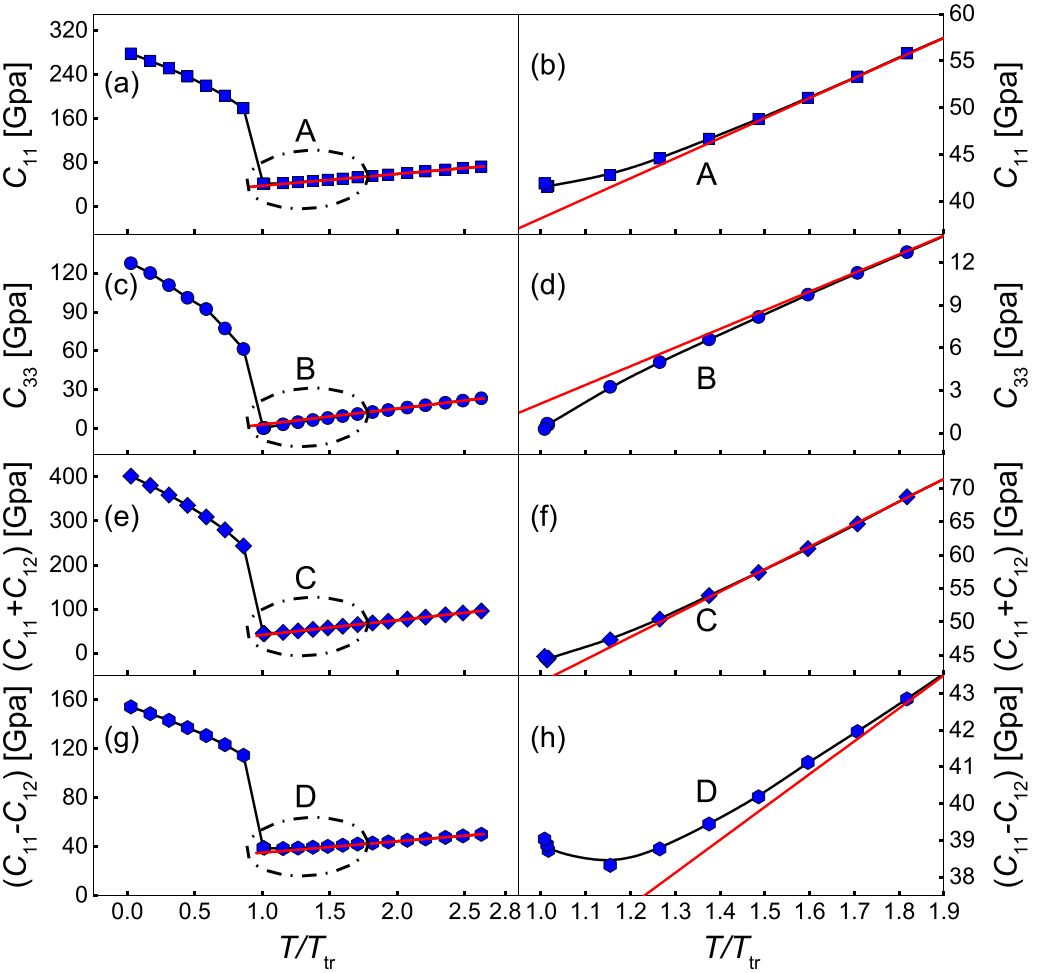

FIG. 4. Temperature evolution of elastic moduli. (b), (d), (f), and (h) are the local magnifications of elastic moduli above T_{tr}, as indicated by A, B, C, and D in (a), (c), (e), and (g), respectively. Elastic moduli increase linearly at $T \gg T_{tr}$.

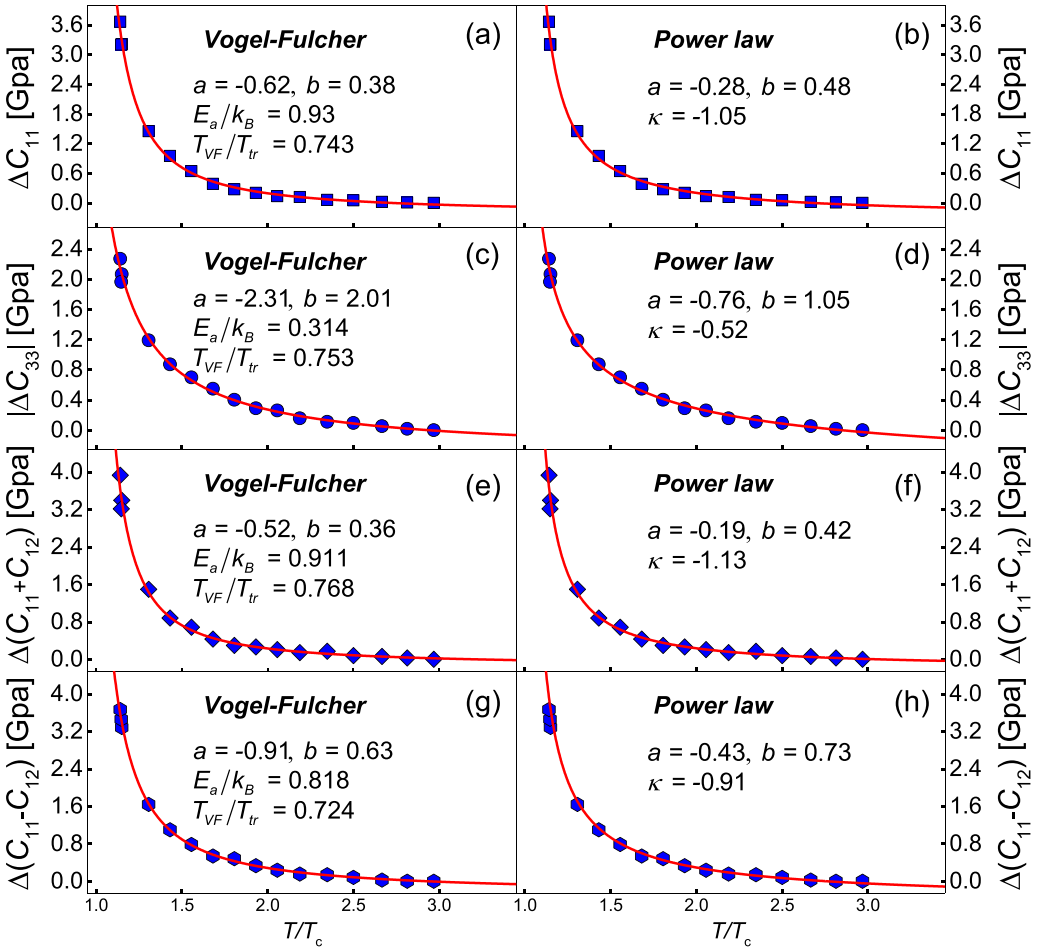

FIG. 5. Fits of precursor elastic softening and hardening for the power-law [Eq. (2)] and Vogel-Fulcher [Eq. (3)] analyses and the parameters indicated in the legends.

Following Cordero *et al.* [31], we fit the evolution of the precursor elastic effect with both a power-law function and a Vogel-Fulcher relation. The power law is

$$\Delta C = a + b\left(\frac{T}{T_{\rm c}} - 1\right)^{\kappa}, \tag{6}$$

where a, b, and κ are properties of the material of interest. The temperature $T_{\rm c}$ is typically slightly below the transition temperature $T_{\rm tr}$. In some scenarios, where local disorder leads to thermally activated dynamics, the elastic softening follows a Vogel-Fulcher statistics with

$$\Delta {\rm C} = a + b\exp\left(\frac{E_a/k_B}{T/T_{\rm tr} - T_{VF}/T_{\rm tr}}\right), \tag{7}$$

where a, b are the materials parameters, $E_{\rm a}$ is the activation energy, and $T_{\rm VF}$ is the Vogel-Fulcher energy.

We found, in our simulations, shear elastic constant softening (ΔC_{33}), tensile elastic constant hardening (ΔC_{11}), and hardening of combinations of C_{11} and C_{12} [$\Delta(C_{11}+C_{12})$ and $\Delta(C_{11}-C_{12})$] can be well described by, alternatively, a power law and Vogel-Fulcher statistics (Fig. 5). In fact, numerical fits to either Eqs. (6) or (7) are virtually impossible to distinguish from the other (Fig. 5). The $T_{\rm c}$ in the power law is 0.32 K, which is slighter lower than $T_{\rm tr} \approx 0.362$ K. As in previous studies [32], it was found impossible to distinguish between the two analytical forms; both give excellent results. The precursor effect can now be followed at higher resolution to temperature as high as $\sim 2.5T_{\rm c}$. Again, the convergence is continuous. There is no indication of a Burns anomaly.

IV. DISCUSSION

The phase transition is characterized by a symmetry-breaking shear instability e_3 and nonsymmetry-breaking components e_1 and e_2. The softening of the elastic moduli is described by a power-law softening or by a Vogel-Fulcher temperature dependence. The Vogel-Fulcher temperatures are almost identical ($T_{\rm VF} = 0.7T_{\rm tr}$), while the Vogel-Fulcher energies differ with the smaller energy for the symmetry-breaking component ($E_{\rm VF} = 0.3k_{\rm B}$) and the higher Vogel-Fulcher energy for the nonsymmetry breaking strain ($E_{\rm VF} = 0.7k_{\rm B} \sim 0.9k_{\rm B}$). The power-law exponents are $\kappa = -0.52$ for the symmetry-breaking strain (e_3) and $\kappa \approx -1.0$ for the nonsymmetry-breaking components [$\kappa \approx -1.05$ for ΔC_{11}, $\kappa \approx -1.13$ for $\Delta(C_{11}+C_{12})$ and $\kappa \approx -0.91$ for $\Delta(C_{11}-C_{12})$, see Figs. 5(b), 5(d), 5(f), and 5(h)].

We can now correlate the precursor effect with the structural changes in the high-temperature phase. The e_3 strain softens because a local, fluctuating nanostructure develops near the onset of softening $\sim 1.8T_{\rm tr}$ and becomes dominant at

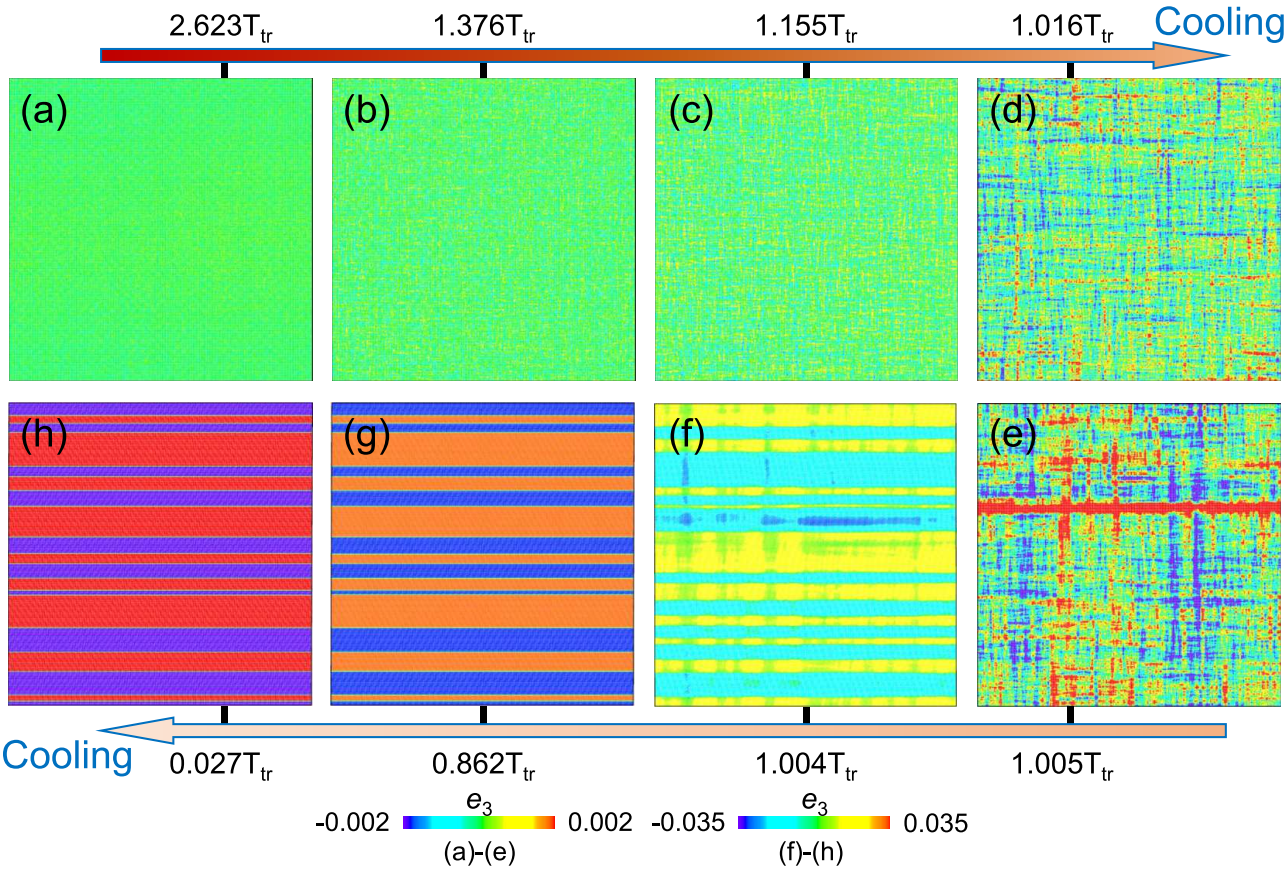

FIG. 6. Temperature evolution of domain structures coded by the primary symmetry-breaking shear strain (e_3).

$T < 1.2T_{tr}$. These nanostructures are very similar to the stable nanostructure in the ferroelastic phase, as shown by the temperature sequences of the domain structures in Fig. 6, which reveal the typical tweedlike ferroelastic patches clearly showing up as the temperature approaches $1.016T_{tr}$ [Fig. 6(d)]. Such tweed appears as an inwoven, fine-scale domain structure, as described in great detail in Refs. [69,70]. The stable nanostructure (the stripe structure) in the ferroelastic phase remains temperature independent once the phase transition has occurred [Figs. 6(g) and 6(h)]. By correlating our fitted results in Figs. 4 and 5 with the temperature evolution of ferroelastic nanostructures in Fig. 6, we can confirm that symmetry-breaking nanostructures soften the elastic moduli in the precursor regime.

We further correlate the precursor hardening of tensile elastic constant ΔC_{22} with the structural changes in the high-temperature phase, as shown by the domain structure evolution coded by atomic-level normal strain e_2 in Fig. 7. The nonsymmetry-breaking strain patterns show very weak structural changes which consist mainly of local density fluctuations, as indicated in Fig. 7 by the local strain patches when the temperature is approaching $1.016T_{tr}$ from above. When the temperature is below T_{tr}, the same secondary strain fluctuations are visible in the ferroelastic phase [Figs. 7(g) and 7(h)], where they are superimposed by the typical strain coupling inside the domain walls that are generated by e_3.

An upper stability point of the precursor effect is now estimated from the structure factor of the total strain deformation or the diffuse scattering Bragg patterns (Fig. 8). Diffraction patterns were calculated from [71]

$$\boldsymbol{I}(\boldsymbol{k}) = \left| \sum_{i=1}^{N} f_i \exp\left(-i\boldsymbol{k} \cdot r_i\right) \right|^2, \tag{8}$$

where I is the diffracted intensity, f_i is the scattering factor of atom i, $\boldsymbol{k}$ is the wave vector, and r_i is the position of atom i. There is only one atom per unit cell in our model, so the scattering factor f_i is uniformly unity. The relevant diffuse scattering Bragg patterns are shown in Figs. 8 and 9. Similar diffuse scattering Bragg patterns have been calculated by Wang *et al.* [72] to investigate the dynamical tweed structure in a defect-free ferroelastic system.

Very weak inhomogeneities can be observed at $2.6T_{tr}$ [Fig. 8(a)], while the effect increases dramatically when T_{tr} is approached [Fig. 8(e)]. The high-resolution structure factors of the (220)* Bragg reflection in Fig. 9 show a similar picture, where a very weak deformation is seen at $2.6T_{tr}$, while the deformation at $1.37T_{tr}$ is already very strong. These results coincide with the power-law fit and Vogel-Fulcher analysis but do not depend on any fitting procedure to determine the temperature scale. We are confident, therefore, that the precursor effect in this simple toy model extends to temperatures as high as $\sim 2T_{tr}$ and becomes clearly visible (say in resonant ultrasound spectroscopy experiments) $< 1.3T_{tr}$.

The power-law exponents in experimental studies cannot be directly compared with our simple toy model because our

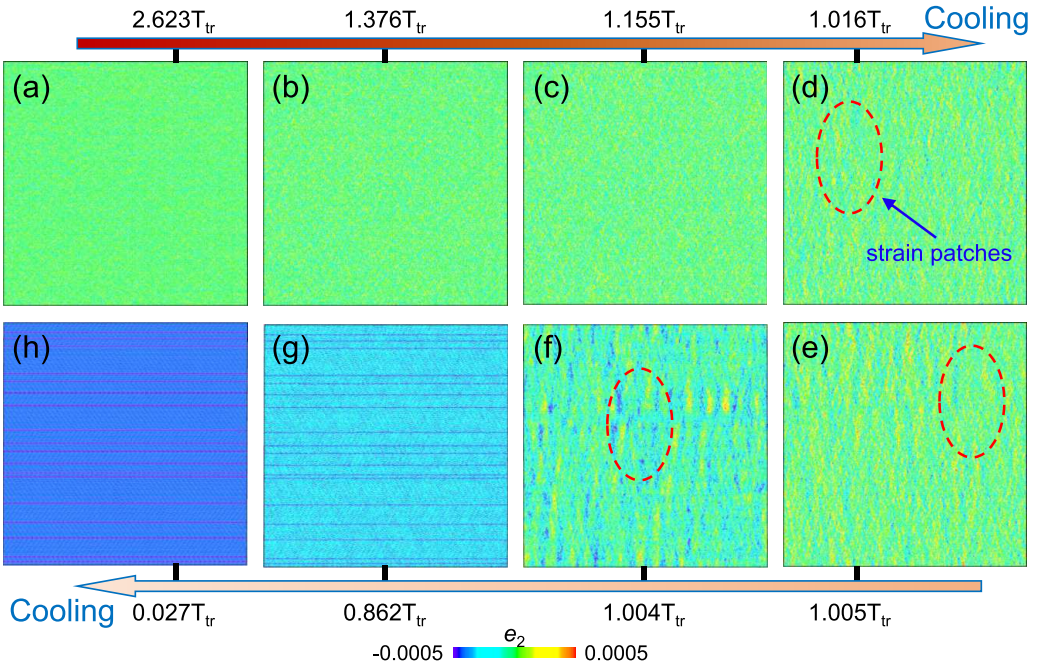

FIG. 7. Temperature evolution of domain structures coded by the secondary nonsymmetry-breaking normal strain (e_2).

model is 2D, and the interatomic interactions are limited to central forces with one atom per unit cell. Experimental [73] softening exponents are $\kappa = -1.5$ for $SrTiO_3$ and $\kappa = -0.3$ for $BaTiO_3$. Similar exponents but with smaller precursor temperature intervals were previously observed in isostructural $KMnF_3$ and $KMn_xCa_{1-x}F_3$ [44,74,75] with values of κ ranging between -0.4 and -1. In $PbSc_{0.5}Ta_{0.5}O_3$ (PST), the exponent is ~ -0.5 [76] with a smaller precursor interval, while ~ -0.3 has recently been found for structural fluctuations in cuprate superconductors [77].

In the simple theory of Carpenter and Salje [1] of the symmetry-breaking modulus, it is argued that, if a single branch flattens significantly as the soft mode decreases in frequency, the result is $\kappa = -1.5$. If two branches flatten while the third remains relatively steep, the result is $\kappa = -1$. If the dispersion of all three branches in three

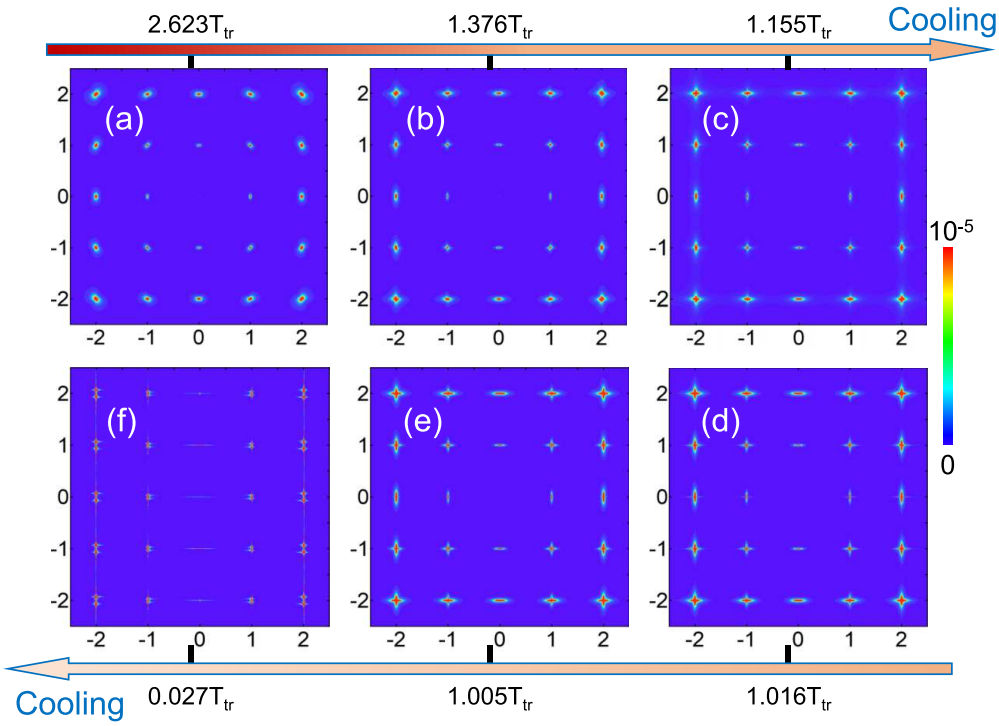

FIG. 8. Temperature evolution of the simulated diffuse scattering.

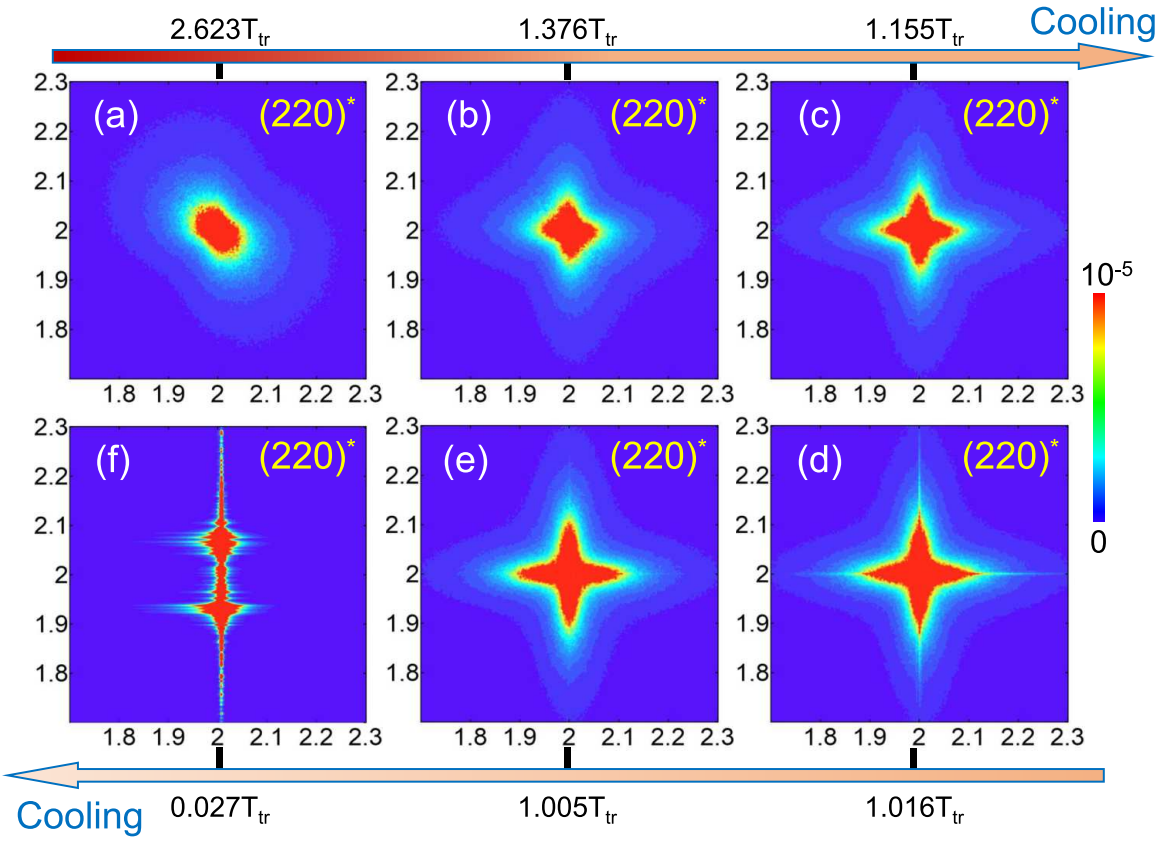

FIG. 9. Temperature evolution of the simulated diffuse scattering around the $(220)^*$ Bragg reflection.

dimensions (3D) reduces with the softening of the soft mode, this leads to $\kappa = -\frac{1}{2}$. In our model, we show that two soft mode branches in 2D yield the approximate exponent $\kappa = -\frac{1}{2}$ for the symmetry-breaking modulus and $\kappa = -1$ for the nonsymmetry-breaking modulus. It is most intriguing that the larger symmetry-breaking strain fluctuations yield a slightly weaker softening of the related modulus ΔC_{33} than the smaller nonsymmetry-breaking strain, which leads to hardening of ΔC_{22}. Structurally, this means that tweed and fluctuating ferroelastic domains in the precursor regime have a relatively smaller effect on the elastic moduli than the weak density fluctuations which harden the structure. It also explains why experimentally observed elastic precursor softening and hardening follow different temperature evolutions, which stems from the different symmetry properties of the related lattice strains. This makes the theoretical interpretation of the experimental results more complex. On the other hand, all results show that the proposed power-law dependence [1] of precursor effects is indeed correct and can be used for quantitative analysis in all ferroic systems with, so far, no known deviations.

ACKNOWLEDGMENTS

G.L. is grateful for the financial support by the National Natural Science Foundation of China (Grant No. 12304130) and the Doctoral Starting Fund of Yantai University (Grant

TABLE I. Planar subgroups of plane group *p4mm* (right hand column) as obtained by analysis of relevant subgroups of space group *P4mm*. IR = irreducible representation; OPD = order parameter direction; basis = conventional basis vectors of the sublattice with respect to lattice vectors of *P4mm*; origin = origin of the space group setting of the subgroup with respect to the origin of the *P4mm*; size = relative size of the primitive unit cell in the parent group and subgroup; index = index of the subgroup relative to *P4mm*; cont. = continuous transition allowed (yes) or not (no); spec. = ferroic character of the transition (pfs = proper ferroelastic; pfc = proper ferroelectric).

IR	OPD	Subgroup	Basis	Origin	Size	Index	Cont.	Spec.	Relevant plane group
Γ_1	P1 (*a*)	99 *P4mm*	(1,0,0), (0,1,0), (0,0,1)	(0,0,0)	1	1	No		*p4mm*
Γ_2	P1 (*a*)	32 *Pmm*2	(1,0,0), (0,1,0), (0,0,1)	(0,0,0)	1	2	Yes	pfs	*p2mm*
Γ_3	P1 (*a*)	35 *Cmm*2	(1,1,0), (−1,1,0), (0,0,1)	(0,0,0)	1	2	Yes	pfs	*c2mm*
Γ_4	P1 (*a*)	75 *P*4	(1,0,0), (0,1,0), (0,0,1)	(0,0,0)	1	2	Yes		*p*4
Γ_5	P1 (*a*,0)	6 *Pm*	(1,0,0), (0,1,0), (0,0,1)	(0,0,0)	1	4	Yes	pfs, pfc	*pm*
Γ_5	P3 (*a*, *a*)	8 *Cm*	(1,1,0), (−1,1,0), (0,0,1)	(0,0,0)	1	4	Yes	pfs, pfc	*cm*
Γ_5	C1 (*a*, *b*)	1 *P*1	(1,0,0), (0,1,0), (0,0,1)	(0,0,0)	1	8	No	pfs, pfc	*p*1

No. 1115-2222006). E.K.H.S. and M.A.C. are grateful to EPSRC (EP/P024904/1) and the EU's Horizon 2020 programme under the Marie Sklodowska-Curie Grant (Grant No. 861153).

APPENDIX: SYMMETRY ANALYSIS OF THE SPRING MODEL

The spring model presented in this paper and previously [78] conforms in its paraelastic (square) phase to the symmetry of plane group *p*4*mm*. This can be seen by taking a square version of Fig. 1, locating the symmetry elements, and comparing with the pattern of symmetry elements shown on p. 186 of the International Tables for Crystallography [79]. Similarly, the ferroelastic phase in Fig. 1 has rectangular symmetry *c*2*mm* with unit cell based on the diagonals in that figure. The plane group *c*2*mm* is a maximal subgroup of *p*4*mm* (Bilbao Crystallographic Server [80]).

To facilitate the analysis of the symmetry properties of the spontaneous strain and elastic moduli, we sought to use the software tools (for space groups) from the Brigham Young ISOTROPY suite [81]. To this end, we identified *P*4*mm* as the space group proxy for plane group *p*4*mm*; this is seen by comparing the diagram for *P*4*mm* (p. 417, Ref. [79]) with that for *p*4*mm* (p. 186, Ref. [79]), or by noting that all Wyckoff positions in *P*4*mm* feature the same z, and the (x, y) follow the same pattern as in *p*4*mm*. Similarly, *Cmm*2 can be seen to be the space group proxy for *c*2*mm*.

Starting then with *P*4*mm*, ISOTROPY was used to examine strains; those with any z component were dropped. ISOSUBGROUP from the ISOTROPY suite was used to list subgroups (as space groups) arising from irreducible representations (irreps) belonging to the Γ point. Finally, the Wyckoff positions were examined, using the Bilbao Server, to find the plane groups corresponding to the space groups listed by ISOSUBGROUP (see table 1 in Ref. [82]). The results of this analysis are given in Table I. Readers are referred to Howard and Stokes [83] for a more detailed explanation of how such symmetry properties are derived in the case of conventional 3D space groups,

The equivalent point group labels of the planar subgroups from Table I are listed in Table II. Maintaining labels that apply to relationships in 3D, there are three possible components in the strain tensor that describe possible lattice distortions of the *p*4*mm* parent structure, e_1, e_2, and e_3. In symmetry-adapted form, they are $e_1 + e_2$ (Γ_1), $e_1 - e_2$ (Γ_2), and e_3 (Γ_3). Here, $e_1 + e_2$ would correspond to a volume strain (an area strain in 2D), while $e_1 - e_2$ and e_3 are shear strains. Likewise,

TABLE II. Notation for the active Γ point representations, their equivalent labels in point group notation, and the resulting subgroups of plane group *p*4*mm*.

Notation from ISOTROPY	Point group notation	Subgroup of *p*4*mm*
Γ_1	A1	*p*4*mm*
Γ_2	B1	*p*2*mm*
Γ_3	B2	*c*2*mm*
Γ_4	A2	*p*4
Γ_5	E	*pm*, *cm*, *p*1

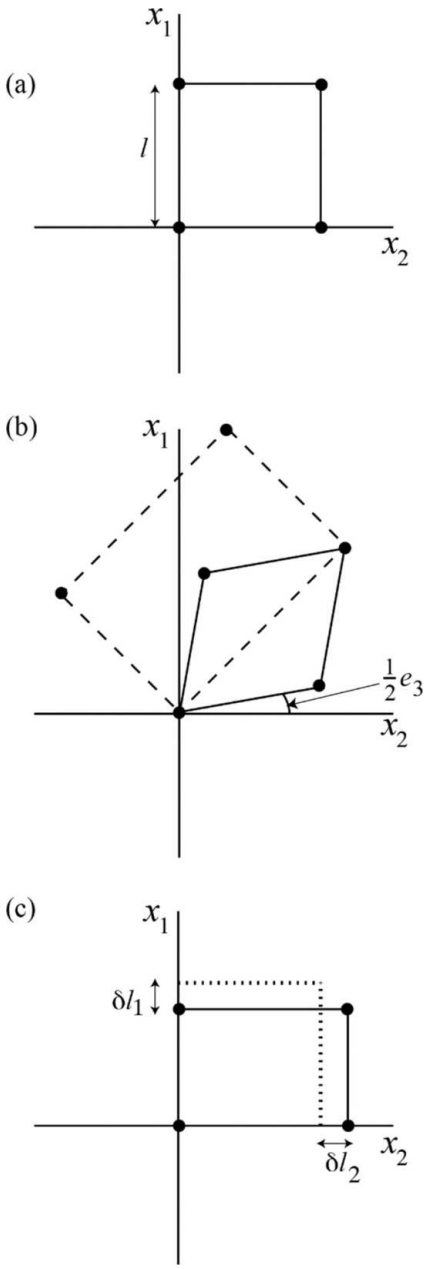

FIG. 10. Relationships between unit cells with respect to orthogonal reference axes x_1, x_2 for (a) *p*4*mm* as the plane group for the parent structure, (b) *c*2*mm* when the order parameter has the symmetry of Γ_3, and (c) *p*2*mm* when the order parameter has the symmetry of Γ_2. In (b), solid lines show the distortion of the primitive parent unit cell, and dashed lines show the conventional C-face-centered cell; the shear strain is e_3. In (c), solid lines show the distorted unit cell and dotted lines the parent cell; linear strains are $e_1 = \delta l_1/l$, $e_2 = \delta l_2/l$.

the parent structure has three nonzero elastic moduli which, in Voigt notation, are

$$\begin{bmatrix} C_{11} & C_{12} & 0 \\ C_{12} & C_{11} & 0 \\ 0 & 0 & C_{33} \end{bmatrix}.$$

In symmetry-adapted form, these become

$$\begin{bmatrix} C_{11}+C_{12} & 0 & 0 \\ 0 & C_{11}-C_{12} & 0 \\ 0 & 0 & C_{33} \end{bmatrix},$$

where $(C_{11} + C_{12})$ is the bulk modulus in 2D with symmetry of Γ_1 (identity), while $(C_{11} - C_{12})$ and C_{33} are shear constants with symmetries of Γ_2 and Γ_3, respectively.

The construction of the spring model is such that there is an in-built elastic instability which leads to a phase transition with Γ_3 as the active representation. The change in plane group is $p4mm \rightarrow c2mm$, and Figs. 10(a) and 10(b) show the relationship between the unit cells of parent and product structures. By analogy with phase transitions in crystals, this would be described as true proper ferroelastic. The symmetry-breaking shear strain is e_3, and the elastic constant expected to go to zero at the critical temperature T_c is C_{33}. Taking e_3 as the order parameter, coupling with the other two strains would have the form $\lambda_1(e_1 + e_2)e_3^2$, and $\lambda_2(e_1 - e_2)^2e_3^2$. In the $c2mm$ structure, the expected strain relationships are then $(e_1 + e_2) \propto e_3^2$ and $(e_1 - e_2) = 0$. Investigation of the spring model has shown that there is a second elastic instability involving weak softening of $(C_{11} - C_{12})$. This would give a transition $p4mm \rightarrow p2mm$, with $(e_1 - e_2)$ as the symmetry-breaking shear strain (Γ_2 active).

The $c2mm$ structure has four nonzero elastic moduli C_{11}, C_{22}, C_{12}, and C_{33}. These are defined with respect to the new axes of the conventional C-face-centered cell, i.e., at 45° to the axes shown in Fig. 10(b), but are not the primary focus of interest in the current analysis. Values of spontaneous shear strains and elastic moduli were determined from the response of the model to stresses applied parallel to x_1 and x_2. In the high-temperature structure, these give values of C_{11} $(= C_{22})$, C_{12}, and C_{33} directly. Once the symmetry is broken, x_1 and x_2 are no longer parallel to symmetry axes of the low-temperature unit cell shown in Fig. 10(b). Strictly speaking, stresses applied in these directions yield responses which are some more complex combinations of the constants of the orthorhombic structure. For this paper, the model stresses were applied parallel and perpendicular to one of the faces of the unit cell of the distorted structure. However, the shear strain e_3 remains small so that the resulting values of constants obtained remain close to C_{11}, C_{22}, and C_{33} of the $c2mm$ structure in its unconventional (primitive) setting. This treatment does not permit analysis of subtle changes of the linear elastic moduli due to coupling with the order parameter, but it does allow focus on the difference in elastic properties parallel and perpendicular to the ferroelastic twin walls that develop as a consequence of the phase transition.

[1] M. A. Carpenter and E. K. H. Salje, Elastic anomalies in minerals due to structural phase transitions, Eur. J. Mineral. **10**, 693 (1998).

[2] H. Pöttker and E. K. H. Salje, Twin boundary profiles with linear-quadratic coupling between order parameters, J. Phys.: Condens. Matter **26**, 342201 (2014).

[3] H. Pöttker and E. K. H. Salje, Flexoelectricity, incommensurate phases and the Lifshitz point, J. Phys.: Condens. Matter **28**, 075902 (2016).

[4] E. K. H. Salje, Ferroelastic materials, Annu. Rev. Mater. Res. **42**, 265 (2012).

[5] E. K. H. Salje and M. A. Carpenter, Linear-quadratic order parameter coupling and multiferroic phase transitions, J. Phys.: Condens. Matter **23**, 462202 (2011).

[6] S. Conti, S. Müller, A. Poliakovsky, and E. K. H. Salje, Coupling of order parameters, chirality, and interfacial structures in multiferroic materials, J. Phys.: Condens. Matter **23**, 142203 (2011).

[7] H. Schneider, J. Schreuer, and B. Hildmann, Structure and properties of mullite—A review, J. Eur. Ceram. Soc. **28**, 329 (2008).

[8] S. Hirotsu, Softening of bulk modulus and negative Poisson's ratio near the volume phase transition of polymer gels, J. Chem. Phys. **94**, 3949 (1991).

[9] L. Mañosa, A. González-Comas, E. Obradó, A. Planes, V. A. Chernenko, V. V. Kokorin, and E. Cesari, Anomalies related to the TA_2-phonon-mode condensation in the Heusler Ni_2MnGa alloy, Phys. Rev. B **55**, 11068 (1997).

[10] R. E. A. McKnight, M. A. Carpenter, T. W. Darling, A. Buckley, and P. A. Taylor, Acoustic dissipation associated with phase transitions in lawsonite, $CaAl_2Si_2O_7(OH)_2{\cdot}H_2O$, Am. Mineral. **92**, 1665 (2007).

[11] T. M. Brill, S. Mittelbach, W. Assmus, M. Mullner, and B. Luthi, Elastic properties of NiTi, J. Phys.: Condens. Matter **3**, 9621 (1991).

[12] M. A. Carpenter, E. K. H. Salje, A. Graeme-Barber, B. Wruck, M. T. Dove, and K. S. Knight, Calibration of excess thermodynamic properties and elastic constant variations associated with the $\alpha \leftrightarrow \beta$ phase transition in quartz, Am. Mineral. **83**, 2 (1998).

[13] Y. Ishibashi, K. Hara, and A. Sawada, The ferroelastic transition in some scheelite-type crystals, Physica B+C **150**, 258 (1988).

[14] T. Ishidate and S. Sasaki, Elastic anomaly and phase transition of $BaTiO_3$, Phys. Rev. Lett. **62**, 67 (1989).

[15] G. Errandonea, Elastic and mechanical studies of the transition in LaP_5O_{14}: A continuous ferroelastic transition with a classical Landau-type behavior, Phys. Rev. B **21**, 5221 (1980).

[16] A. V. Kityk, W. Schranz, P. Sondergeld, D. Havlik, E. K. H. Salje, and J. F. Scott, Low-frequency superelasticity and nonlinear elastic behavior of $SrTiO_3$ crystals, Phys. Rev. B **61**, 946 (2000).

[17] F. Cordero, F. Craciun, F. Trequattrini, and C. Galassi, Piezoelectric softening in ferroelectrics: Ferroelectric versus antiferroelectric $PbZr_{1-x}Ti_xO_3$, Phys. Rev. B **93**, 174111 (2016).

[18] F. Cordero, Piezoelectricity from elastic and dielectric measurements on unpoled ferroelectrics, Mater. Res. **21**, e20170852 (2018).

[19] A. N. Morozovska, E. A. Eliseev, G. S. Svechnikov, and S. V. Kalinin, Mesoscopic mechanism of the domain wall interaction with elastic defects in uniaxial ferroelectrics, J. App. Phys. **113**, 187203 (2013).

[20] E. K. H. Salje, H. Zhang, H. Idrissi, D. Schryvers, M. A. Carpenter, X. Moya, and A. Planes, Mechanical resonance of the austenite/martensite interface and the pinning of the

martensitic microstructures by dislocations in $Cu_{74.08}Al_{23.13}Be_{2.79}$, Phys. Rev. B **80**, 134114 (2009).
[21] X. He, S. Li, X. Ding, J. Sun, S. Kustov, and E. K. H. Salje, Internal friction in complex ferroelastic twin patterns, Acta Mater. **228**, 117787 (2022).
[22] W. T. Lee, E. K. H. Salje, L. Goncalves-Ferreira, M. Daraktchiev, and U. Bismayer, Intrinsic activation energy for twin-wall motion in the ferroelastic perovskite $CaTiO_3$, Phys. Rev. B **73**, 214110 (2006).
[23] W. T. Lee, E. K. H. Salje, and U. Bismayer, Influence of point defects on the distribution of twin wall widths, Phys. Rev. B **72**, 104116 (2005).
[24] L. Goncalves-Ferreira, S. A. T. Redfern, E. Artacho, E. Salje, and W. T. Lee, Trapping of oxygen vacancies in the twin walls of perovskite, Phys. Rev. B **81**, 024109 (2010).
[25] D. Ertaş and D. R. Nelson, Irreversibility, mechanical entanglement and thermal melting in superconducting vortex crystals with point impurities, Physica C **272**, 79 (1996).
[26] T. Giamarchi and P. Le Doussal, Elastic theory of flux lattices in the presence of weak disorder, Phys. Rev. B **52**, 1242 (1995).
[27] J. Chrosch and E. K. H. Salje, Temperature dependence of the domain wall width in $LaAlO_2$, J. Appl. Phys. **85**, 722 (1999).
[28] B. Wruck, E. K. H. Salje, M. Zhang, T. Abraham, and U. Bismayer, On the thickness of ferroelastic twin walls in lead phosphate $Pb_3(PO_4)_2$ an x-ray diffraction study, Phase Transit. **48**, 135 (1994).
[29] R. J. Harrison and S. A. T. Redfern, The influence of transformation twins on the seismic-frequency elastic and anelastic properties of perovskite: Dynamical mechanical analysis of single crystal $LaAlO_2$, Phys. Earth Planet. In. **134**, 253 (2002).
[30] H. Küpfer, A. A. Zhukov, A. Will, W. Jahn, R. Meier-Hirmer, T. Wolf, V. I. Voronkova, M. Kläser, and K. Saito, Anisotropy in the irreversible behavior of pointlike defects and twins in $YBa_2Cu_3O_{7-\delta}$ single crystals with a peak effect, Phys. Rev. B **54**, 644 (1996).
[31] F. Cordero, F. Trequattrini, P. S. da Silva, M. Venet, O. Aktas, and E. K. H. Salje, Elastic precursor effects during $Ba_{1-x}Sr_xTiO_3$ ferroelastic phase transitions, Phys. Rev. Res. **5**, 013121 (2023).
[32] P. Sollich, V. Heine, and M. T. Dove, The Ginzburg interval in soft-mode phase transitions: Consequences of the rigid unit mode picture, J. Phys.: Condens. Matter **6**, 3171 (1994).
[33] S. di Santo, P. Villegas, R. Burioni, and M. A. Muñoz, Landau-Ginzburg theory of cortex dynamics: Scale-free avalanches emerge at the edge of synchronization, Proc. Natl. Acad. Sci. USA **115**, E1356 (2018).
[34] E. Salje and B. Wruck, Specific-heat measurements and critical exponents of the ferroelastic phase transition in $Pb_3(PO_4)_2$ and $Pb_3(P_{1-x}As_xO_4)_2$, Phys. Rev. B **28**, 6510 (1983).
[35] O. Aktas, M. Kangama, G. Linyu, G. Catalan, X. Ding, A. Zunger, and E. K. H. Salje, Piezoelectricity in nominally centrosymmetric phases, Phys. Rev. Res. **3**, 043221 (2021).
[36] O. I. Malyi, X.-G. Zhao, and A. Zunger, Insulating band gaps both below and above the Néel temperature in d-electron $LaTiO_3$, $SrMnO_3$, and $LaMnO_3$ perovskites as a symmetry-breaking event, Phys. Rev. Mater. **7**, 074406 (2023).
[37] O. I. Malyi and A. Zunger, Rise and fall of Mott insulating gaps in $YNiO_3$ paramagnets as a reflection of symmetry breaking and remaking, Phys. Rev. Mater. **7**, 044409 (2023).
[38] X.-G. Zhao, O. I. Malyi, S. J. L. Billinge, and A. Zunger, Intrinsic local symmetry breaking in nominally cubic paraelectric $BaTiO_3$, Phys. Rev. B **105**, 224108 (2022).
[39] E. K. H. Salje, Elastic softening of zircon by radiation damage, Appl. Phys. Lett. **89**, 131902 (2006).
[40] E. K. H. Salje, D. J. Safarik, J. C. Lashley, L. A. Groat, and U. Bismayer, Elastic softening of metamict titanite $CaTiSiO_5$: Radiation damage and annealing, Am. Mineral. **96**, 1254 (2011).
[41] X.-G. Zhao, G. M. Dalpian, Z. Wang, and A. Zunger, Polymorphous nature of cubic halide perovskites, Phys. Rev. B **101**, 155137 (2020).
[42] O. Aktas, E. K. H. Salje, S. Crossley, G. I. Lampronti, R. W. Whatmore, N. D. Mathur, and M. A. Carpenter, Ferroelectric precursor behavior in $PbSc_{0.5}Ta_{0.5}O_3$ detected by field-induced resonant piezoelectric spectroscopy, Phys. Rev. B **88**, 174112 (2013).
[43] O. Aktas, M. Kangama, G. Linyu, X. Ding, M. A. Carpenter, and E. K. H. Salje, Probing the dynamic response of ferroelectric and ferroelastic materials by simultaneous detection of elastic and piezoelectric properties, J. Alloy. Compd. **903**, 163857 (2022).
[44] W. Cao and G. R. Barsch, Elastic constants of $KMnF_3$ as functions of temperature and pressure, Phys. Rev. B **38**, 7947 (1988).
[45] E. Pytte, Soft-mode damping and ultrasonic attenuation at a structural phase transition, Phys. Rev. B **1**, 924 (1970).
[46] J. D. Axe and G. Shirane, Study of the α-β quartz phase transformation by inelastic neutron scattering, Phys. Rev. B **1**, 342 (1970).
[47] U. T. Höchli, Elastic constants and soft optical modes in gadolinium molybdate, Phys. Rev. B **6**, 1814 (1972).
[48] W. Rehwald, The study of structural phase transitions by means of ultrasonic experiments, Adv. Phys. **22**, 721 (1973).
[49] H. Z. Cummins, A. D. Buckingham, G. W. Series, E. R. Pike, and J. G. Powles, Brillouin scattering spectroscopy of ferroelectric and ferroelastic phase transitions, Philos. Trans. R. Soc. A **293**, 393 (1997).
[50] W. Yao, H. Z. Cummins, and R. H. Bruce, Acoustic anomalies in terbium molybdate near the improper ferroelastic-ferroelectric phase transition, Phys. Rev. B **24**, 424 (1981).
[51] J. O. Fossum, A phenomenological analysis of ultrasound near phase transitions, J. Phys. C: Solid State Phys. **18**, 5531 (1985).
[52] Z. Zhao, X. Ding, T. Lookman, J. Sun, and E. K. H. Salje, Mechanical loss in multiferroic materials at high frequencies: Friction and the evolution of ferroelastic microstructures, Adv. Mater. **25**, 3244 (2013).
[53] G. Lu, X. Ding, J. Sun, and E. K. H. Salje, Wall-wall and kink-kink interactions in ferroelastic materials, Phys. Rev. B **106**, 144105 (2022).
[54] G. Lu, K. Hideo, X. Ding, Z. Xu, R. Chu, G. F. Nataf, and E. K. H. Salje, Influence of kinks on the interaction energy between ferroelastic domain walls in membranes and thin films, Microstructures **3**, 2023033 (2023).
[55] G. Lu, S. Li, X. Ding, and E. K. H. Salje, Piezoelectricity and electrostriction in ferroelastic materials with polar twin boundaries and domain junctions, Appl. Phys. Lett. **114**, 202901 (2019).
[56] G. Lu, S. Li, X. Ding, J. Sun, and E. K. H. Salje, Enhanced piezoelectricity in twinned ferroelastics with nanocavities, Phys. Rev. Mater. **4**, 074410 (2020).

[57] G. Lu, S. Li, X. Ding, J. Sun, and E. K. H. Salje, Ferroelectric switching in ferroelastic materials with rough surfaces, Sci. Rep. **9**, 15834 (2019).

[58] G. Lu, S. Li, X. Ding, J. Sun, and E. K. H. Salje, Current vortices and magnetic fields driven by moving polar twin boundaries in ferroelastic materials, npj Comput. Mater. **6**, 145 (2020).

[59] G. Catalan, J. Seidel, R. Ramesh, and J. F. Scott, Domain wall nanoelectronics, Rev. Mod. Phys. **84**, 119 (2012).

[60] S. A. Hayward and E. K. H. Salje, Cubic-tetragonal phase transition in $SrTiO_3$ revisited: Landau theory and transition mechanism, Phase Transit. **68**, 501 (1999).

[61] G. Lu, S. Li, X. Ding, J. Sun, and E. K. H. Salje, Electrically driven ferroelastic domain walls, domain wall interactions, and moving needle domains, Phys. Rev. Mater. **3**, 114405 (2019).

[62] E. K. H. Salje, S. Li, M. Stengel, P. Gumbsch, and X. Ding, Flexoelectricity and the polarity of complex ferroelastic twin patterns, Phys. Rev. B **94**, 024114 (2016).

[63] S. Plimpton, Fast parallel algorithms for short-range molecular dynamics, J. Comput. Phys. **117**, 1 (1995).

[64] A. Stukowski, Visualization and analysis of atomistic simulation data with OVITO—The open visualization tool, Model. Simul. Mater. Sc. **18**, 015012 (2010).

[65] S. Nosé, A unified formulation of the constant temperature molecular dynamics methods, J. Chem. Phys. **81**, 511 (1984).

[66] W. G. Hoover, Canonical dynamics: Equilibrium phase-space distributions, Phys. Rev. A **31**, 1695 (1985).

[67] E. K. H. Salje, B. Wruck, and H. Thomas, Order-parameter saturation and low-temperature extension of Landau theory, Z. Phys. B: Condens. Matter. **82**, 399 (1991).

[68] G. Burns and F. H. Dacol, Polarization in the cubic phase of $BaTiO_3$, Solid State Commun. **42**, 9 (1982).

[69] D. D. Viehland and E. K. H. Salje, Domain boundary-dominated systems: Adaptive structures and functional twin boundaries, Adv. Phys. **63**, 267 (2014).

[70] E. Salje and K. Parlinski, Microstructures in high T_c superconductors, Supercond. Sci. Technol. **4**, 93 (1991).

[71] C. S. Becquart, P. C. Clapp, and J. A. Rifkin, Molecular-dynamics simulation of tweed structure and the ω phase in Ni-Al, Phys. Rev. B **48**, 6 (1993).

[72] X. Wang, E. K. H. Salje, J. Sun, and X. Ding, Glassy behavior and dynamic tweed in defect-free multiferroics, Appl. Phys. Lett. **112**, 012901 (2018).

[73] B. Zalar, A. Lebar, J. Seliger, R. Blinc, V. V. Laguta, and M. Itoh, NMR study of disorder in $BaTiO_3$ and $SrTiO_3$, Phys. Rev. B **71**, 064107 (2005).

[74] W. Schranz, P. Sondergeld, A. V. Kityk, and E. K. H. Salje, Dynamic elastic response of $KMn_{1-x}Ca_xF_3$: Elastic softening and domain freezing, Phys. Rev. B **80**, 094110 (2009).

[75] E. K. H. Salje and H. Zhang, Domain boundary pinning and elastic softening in $KMnF_3$ and $KMn_{1-x}Ca_xF_3$, J. Phys-Condens. Mat. **21**, 035901 (2009).

[76] G. Linyu, F. J. Romero, V. Franco, J.-M. Martín-Olalla, M. C. Gallardo, E. K. H. Salje, Y. Zhou, and O. Aktas, Correlations between elastic, calorimetric, and polar properties of ferroelectric $PbSc_{0.5}Ta_{0.5}O_3$ (PST), Appl. Phys. Lett. **115**, 161904 (2019).

[77] D. Pelc, R. J. Spieker, Z. W. Anderson, M. J. Krogstad, N. Biniskos, N. G. Bielinski, B. Yu, T. Sasagawa, L. Chauviere, P. Dosanjh *et al.*, Unconventional short-range structural fluctuations in cuprate superconductors, Sci. Rep. **12**, 20483 (2022).

[78] E. K. H. Salje, X. Ding, Z. Zhao, T. Lookman, and A. Saxena, Thermally activated avalanches: Jamming and the progression of needle domains, Phys. Rev. B **83**, 104109 (2011).

[79] *International Tables for Crystallography*, 6th ed., edited by M. I. Aroyo (Wiley, Hoboken, 2016), Vol. A.

[80] https://www.cryst.ehu.es.

[81] https://iso.byu.edu/iso/isotropy.php.

[82] D. M. Hatch, T. Lookman, A. Saxena, and S. R. Shenoy, Proper ferroelastic transitions in two dimensions: Anisotropic long-range kernels, domain wall orientations, and microstructure, Phys. Rev. B **68**, 104105 (2003).

[83] C. J. Howard and H. T. Stokes, Structures and phase transitions in perovskites—A group-theoretical approach, Acta Cryst. A **61**, 93 (2005).